

## Orbits in a non-Kerr Dynamical System

G. Contopoulos

*Research Center for Astronomy, Academy of Athens  
Soranou Efessiou 4, GR-11527, Athens, GREECE  
gcontop@academyofathens.gr*

G. Lukes-Gerakopoulos

*Research Center for Astronomy, Academy of Athens  
Soranou Efessiou 4, GR-11527, Athens, GREECE  
gglukes@phys.uoa.gr*

T. A. Apostolatos

*Section of Astrophysics, Astronomy, and Mechanics,  
Department of Physics, University of Athens  
Panepistimiopolis Zografos GR15783, Athens, Greece  
thapostol@phys.uoa.gr*

Received (to be inserted by publisher)

We study the orbits in a Manko-Novikov type metric (MN) which is a perturbed Kerr metric. There are periodic, quasi-periodic, and chaotic orbits, which are found in configuration space and on a surface of section for various values of the energy  $E$  and the  $z$ -component of the angular momentum  $L_z$ . For relatively large  $L_z$  there are two permissible regions of non-plunging motion bounded by two closed curves of zero velocity (CZV), while in the Kerr metric there is only one closed CZV of non-plunging motion. The inner permissible region of the MN metric contains mainly chaotic orbits, but it contains also a large island of stability. When  $L_z$  decreases the two permissible regions join and chaos increases. Below a certain value of  $L_z$  most orbits escape inwards and plunge through the horizon. On the other hand as the energy  $E$  decreases (for fixed  $L_z$ ) the outer permissible region shrinks and disappears. In the inner permissible region chaos increases and for sufficiently small  $E$  most orbits are plunging. We find the positions of the main periodic orbits as functions of  $L_z$  and  $E$ , and their bifurcations. Around the main periodic orbit of the outer region there are islands of stability that do not appear in the Kerr metric (integrable case). In a realistic binary system, because of the gravitational radiation, the energy  $E$  and the angular momentum  $L_z$  of an inspiraling compact object decrease and therefore the orbit of the object is non-geodesic. In fact in an extreme mass ratio inspiraling (EMRI) system the energy  $E$  and the angular momentum  $L_z$  decrease adiabatically and therefore the motion of the inspiraling object is characterized by the fundamental frequencies which are drifting slowly in time. In the Kerr metric the ratio of the fundamental frequencies changes strictly monotonically in time. However, in the MN metric when an orbit is trapped inside an island the ratio of the fundamental frequencies remains constant for some time. Hence, if such a phenomenon is observed this will indicate that the system is non integrable and therefore the central object is not a Kerr black hole.

*Keywords:* Kerr black holes; perturbed integrable systems; Birkhoff islands

## 1. Introduction

The geodesics in a Kerr metric are derived from an integrable system of equations. The Kerr metric itself is characterized by its mass  $M$  and spin  $S$ . However, there are other solutions of the vacuum Einstein equations, that are close to the Kerr solution, in which the geodesic equations of motion are nonintegrable. The geodesic motions in such backgrounds are either ordered or chaotic. It would be of great interest to check whether the massive compact objects that lie at the center of galaxies are Kerr black holes or some other type of exotic objects (see e.g. [Johannsen & Psaltis, 2010a,b]). This could be attained by analyzing the gravitational waves emitted by a compact object (of mass  $1 - 10^2 M_\odot$ ) inspiraling around the central massive object (with mass  $10^5 - 10^9 M_\odot$ ) that lies at the center of a galaxy; such binary systems are called EMRIs (Extreme Mass Ratio Inspirals). It is expected that future low-frequency detectors of gravitational waves, like the space detector LISA [Bender et al., 1998], will provide us sufficient amount of information, by analyzing the spectrum of the gravitational-wave signal, to answer the question whether the central body is a Kerr black hole or any other kind of a non-Kerr object.

In order to make this distinction more clear we should analyze in detail all types of geodesic orbits in a generic non-Kerr background and focus mainly on the qualitative differences from the corresponding orbits in a Kerr system.

Although there is a variety of vacuum solutions of Einstein equations that could be used as background metrics to study non-Kerr geodesics we have used a specific family of asymptotically flat spacetimes that incorporates the basic characteristics of a generic metric that could be formed as a deviation from the Kerr metric. The particular family MN is a one-parameter subfamily of the so-called Manko-Novikov multiparametric family of metrics [Manko & Novikov, 1992]. The Manko-Novikov family of spacetimes was actually constructed to describe the exterior vacuum of any axisymmetric object one could consider. By setting the value of the new parameter of MN equal to zero we get back the Kerr metric and that is why the MN metric was named by Gair et al [Gair et al., 2008] a “bumpy black hole spacetime (it should be emphasized though that there are infinite ways to create bumpy black hole spacetimes, and MN is simply one of those). The orbits in this metric were first studied in [Gair et al., 2008] and more thoroughly later in [Apostolatos et al., 2009; Lukes-Gerakopoulos et al., 2010]. In the present paper we study in a more systematic way the orbits in a MN metric for a great variety of parameter values and we discuss their effects on the spectrum of the corresponding gravitational waves.

The form of the MN metric is given in [Gair et al., 2008; Lukes-Gerakopoulos et al., 2010]. We do not reproduce it here because it is given by a rather long and complicated formula, which is used by our numerical code in order to solve the geodesic equations for a test particle in the corresponding background.

The MN metric is assumed to have the same mass  $M$  and spin  $S$  as the corresponding Kerr metric, while its quadrupole moment

$$M_2 = -M \left[ \left( \frac{S}{M} \right)^2 + q M^2 \right] \quad (1)$$

differs from the corresponding Kerr moment  $M_{2,K} = -S^2/M$  by the quantity  $-q M^3$ , where  $q$  is the new parameter of the MN metric that produces the deviation of the MN metric from the corresponding Kerr metric. Actually all higher than the quadrupole multipole moments are different from the corresponding multipole moments of Kerr as well when  $q$  is non-zero. If  $q = 0$  the MN metric is reduced to Kerr. In the present paper we consider only the case  $q > 0$ , which corresponds to an oblate perturbation of the Kerr metric.

In section 2 we study systematically the orbits for a wide range of parameter values of the MN metric. In section 3 we study the characteristics of the main periodic orbits. In section 4 we focus our attention on the effects of the non geodesic orbits on the corresponding gravitational waves through which one could in principle distinguish a non-Kerr from a Kerr metric. Finally in section 5 we draw our conclusions.

## 2. Orbits in the Manko-Novikov (MN) metric

In the framework of General Relativity the Einstein field equations play the role of the classical Poisson equation for a given mass and energy distribution. The metric of the spacetime induced by such a distri-

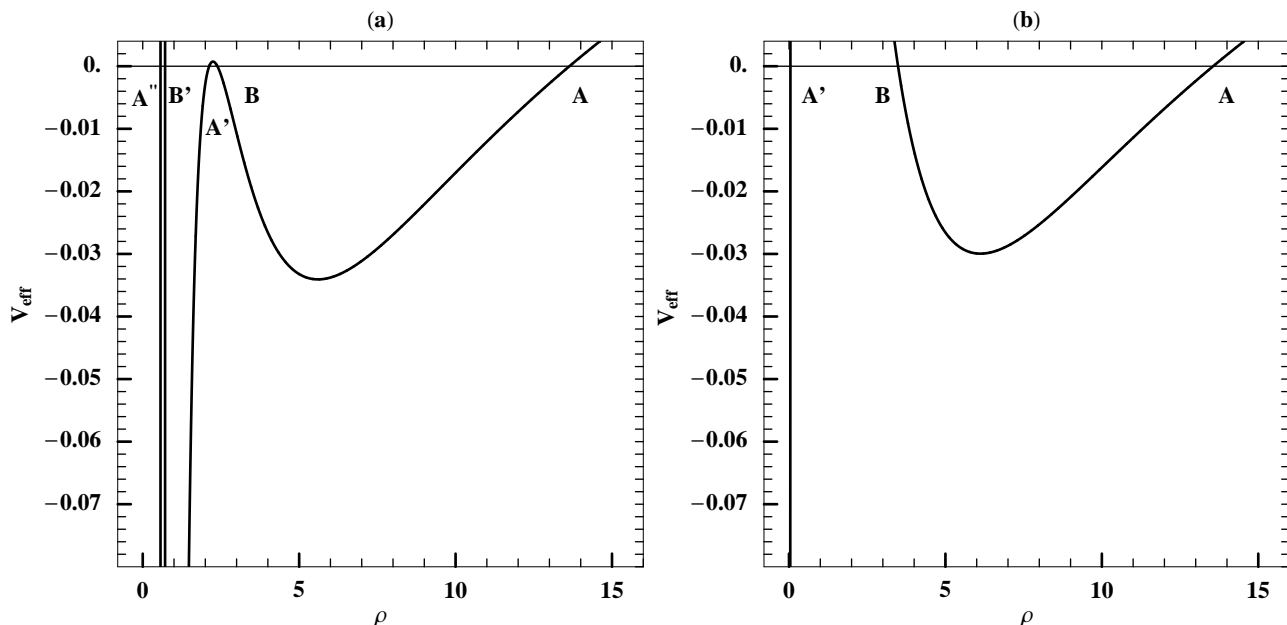


Fig. 1. (a) The effective potential  $V_{\text{eff}}$  as a function of  $\rho$ , for  $z = 0$  (on the equatorial plane) and  $E = 0.95$ ,  $L_z = 3$ ,  $q = 0.95$ ,  $\chi = 0.9$ ,  $M = 1$ . (b) The corresponding  $V_{\text{eff}}$  in the Kerr case ( $q = 0$ ).

bution determines the geodesics followed by the test particles, in analogy with the trajectories followed by test particles in a given “classical” gravitational potential. One of the well-known and astrophysically relevant vacuum solutions of the Einstein field equations is the Kerr metric, which is characterized uniquely by a mass and an angular momentum. A broader family of vacuum solutions of Einstein equations, known as Manko-Novikov (MN) solutions, depend on one more parameter than Kerr, the quadrupole-deviation parameter  $q$ . By setting  $q = 0$  we obtain the Kerr solution. This new metric can be used to describe approximately the exterior of an axisymmetric object that has a finite distribution of mass and angular momentum, and it would be crucial if we could somehow detect qualitative differences in the geodesics between the two types of metrics.

In the following we use the Weyl-Pappapetrou line element expressed in cylindrical coordinates  $(t, \rho, z, \phi)$  to describe the orbits (see e.g. [Gair et al., 2008] or [Lukes-Gerakopoulos et al., 2010]). The MN system has an axis of symmetry  $z$  and a plane of symmetry  $z = 0$ . Thus we consider orbits on the meridian plane  $(\rho, z)$ , while the azimuth  $\phi$  can be easily computed from  $\rho(\tau)$  and  $z(\tau)$  (see [Lukes-Gerakopoulos et al., 2010]), where  $\tau$  is the proper time.

The MN is a stationary axisymmetric metric, thus the geodesic orbits are characterized by two integrals of motion: the energy  $E = -p_t$  and the  $z$ -component of the angular momentum  $L_z = p_z$ . The test mass  $\mu$  of the orbiting body is also fixed and is represented by the constancy of the Hamiltonian function itself. In order to study various types of geodesic orbits we have assumed fixed values for the mass ( $M = 1$ ) and the spin ( $S = 0.9 M^2$ ) of the metric, while we have chosen various values for the orbital parameters  $E, L_z$  and the quadrupolar parameter  $q$ . By choosing  $M = 1$  the dimensionless spin parameter  $\chi = S/M^2$  is equal to the spin  $S$  itself.

The velocities  $\dot{\rho}$  and  $\dot{z}$  satisfy an equation analogous to a generic 2-dimensional Newtonian problem under conservative forces

$$\frac{1}{2}(\dot{\rho}^2 + \dot{z}^2) + V_{\text{eff}}(\rho, z) = 0 \quad (2)$$

where  $V_{\text{eff}}$  is an effective potential that depends on the coordinates  $\rho, z$ , the constants of motion  $E, L_z$ , and the parameters of the metric  $M, S, q$  (see [Lukes-Gerakopoulos et al., 2010] for details). A test particle is allowed to move only in the regions where  $V_{\text{eff}} \leq 0$ . The boundaries of these regions are the so called

CZVs (curves of zero velocity) since there the orbits assume zero velocity ( $\dot{z} = \dot{\rho} = 0$ ). For  $z = 0$  (along the equatorial plane) the effective potential  $V_{\text{eff}}$  as a function of  $\rho$  has the form shown in Fig. 1a. The corresponding allowed region for an orbit is either between  $A$  and  $B$ , or between  $A'$  and  $B'$ , or between  $A''$  and  $\rho = 0$ . The corresponding effective potential in the Kerr case is shown in Fig. 1b. In the Kerr case  $\rho$  can vary either between  $A$  and  $B$ , or between  $A'$  and  $\rho = 0$ . The allowed regions that include the  $\rho = 0$  point correspond to plunging orbits, that is to orbits that will end up plunging to the central singularity of the metric.

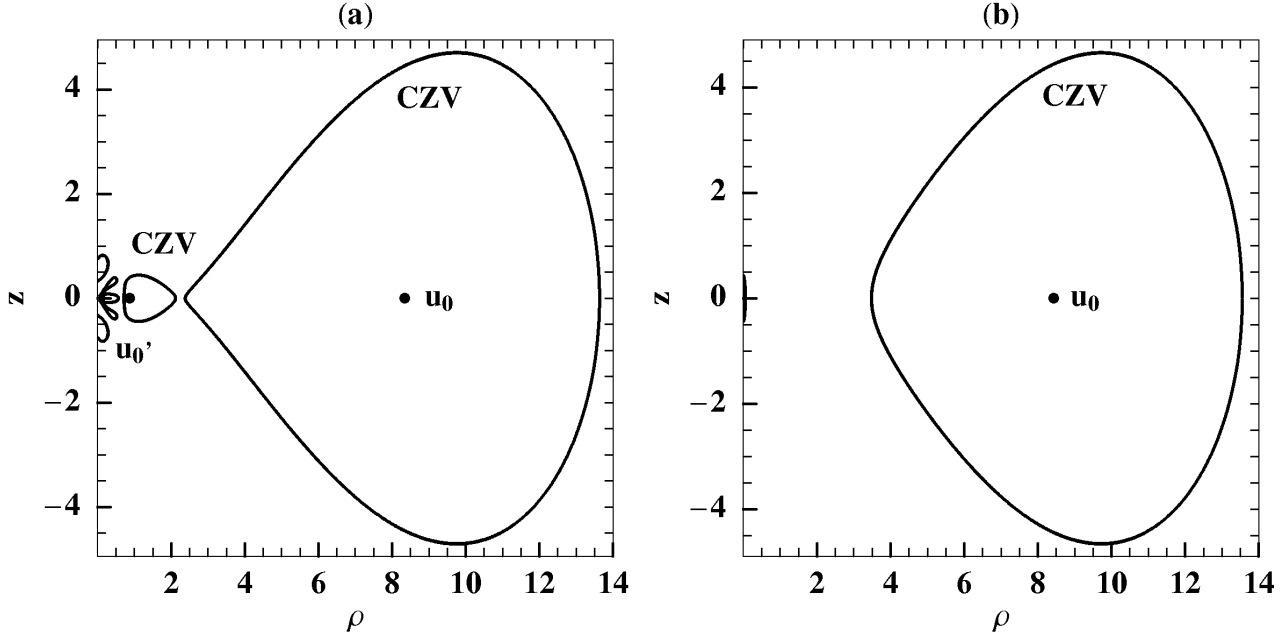


Fig. 2. (a) The permissible regions (inside the CZVs) of the motion on the meridian plane  $(\rho, z)$  for the parameters  $E = 0.95$ ,  $L_z = 3$ ,  $q = 0.95$ ,  $\chi = 0.9$  and  $M = 1$ . (b) The permissible region in the corresponding Kerr case ( $q = 0$ ; all other parameters as in (a)).

For a certain range of parameters there are two distinct closed CZVs within which there are bound geodesic orbits. The central points  $\mathbf{u}_0$  ( $\rho \approx 8.35$ ,  $z = 0$ ) and  $\mathbf{u}'_0$  ( $\rho \approx 0.886$ ,  $z = 0$ ), corresponding to the values of the parameters shown in Fig. 2a, represent the initial conditions (along  $\dot{\rho} = 0$ ) for the two main periodic orbits shown in Figs. 3c,d. These orbits oscillate periodically around the equatorial plane  $z = 0$ . Close to  $\rho = 0$  there are five more CZV curves that are in contact with the neighborhood of  $\rho = 0$ . Orbits inside these CZVs eventually plunge through the horizon which lies along the segment  $\rho = 0$ ,  $|z| \leq k$ , where

$$k = M \frac{\chi^2 - (\sqrt{\chi^2 - 1} - \chi)^2}{\chi^2 + (\sqrt{\chi^2 - 1} - \chi)^2} \quad (3)$$

The horizon of the MN metric is not fully enclosing the central singularity. Therefore the fact that the MN metric is not characterized only by its mass and spin, but also by its oblateness  $q$ , is compatible with the no-hair theorem. In fact the horizon of MN is cut by a line singularity across the equatorial line  $\rho = z = 0$  [Gair et al., 2008], while this singularity does not exist in the case of the Kerr metric. As mentioned before the Kerr metric has only one closed CZV around the point  $\mathbf{u}_0$  ( $\rho \approx 8.44$ ,  $z = 0$ ) corresponding to the values of the parameters shown in Figs. 2a,b). The  $\mathbf{u}_0$  point marks the initial condition (with  $\dot{\rho} = 0$ ) for the periodic orbit in Kerr.

Inside the outer CZV of the MN metric most orbits are ordered (Fig. 3b), while in the inner CZV most orbits are chaotic (Fig. 3a). A method to distinguish between ordered and chaotic orbits is by considering

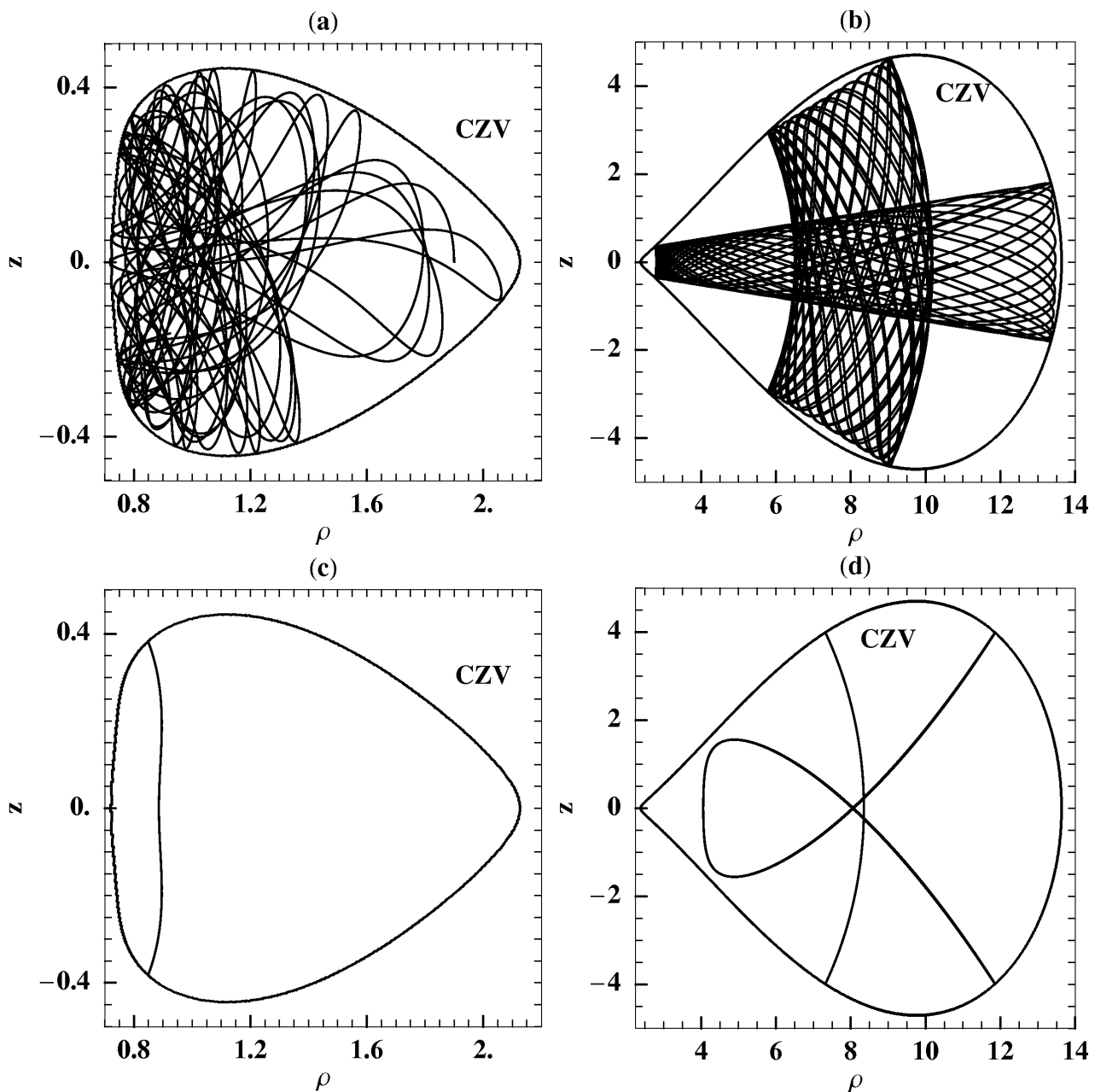


Fig. 3. (a) A chaotic orbit inside the inner CZV of Fig. 2a. (b) Two ordered orbits inside the outer CZV of Fig. 2a. (c) The periodic orbit starting from the point  $\mathbf{u}'_0$ . (d) The periodic orbit starting from the point  $\mathbf{u}_0$ , and a periodic orbit of multiplicity 3 on the surface of section  $z = 0$ . Note that only the edge points of the latter orbit touch the CZV.

a Poincaré surface of section, i.e. a surface intersecting all the orbits in phase space and finding the successive intersections of every orbit by this surface. The successive intersections of an ordered orbit are along a curve that is called invariant curve (Fig. 4), while the successive iterates of a chaotic orbit are scattered irregularly. The invariant curves either encircle the central periodic orbit (the one that passes through the point  $\mathbf{u}_0$  with  $\dot{\rho} = 0$ ) or form a chain of islands of stability around stable resonant periodic orbits. In Fig. 4 we see 3 islands of stability around a resonant orbit (resonance  $2/3$ ), and 2 couples of islands around 2 different resonant periodic orbits of the resonance  $1/2$ . Between the 3 islands of stability there are 3 points corresponding to an unstable periodic orbit of the  $2/3$  resonance. Between the 4 islands

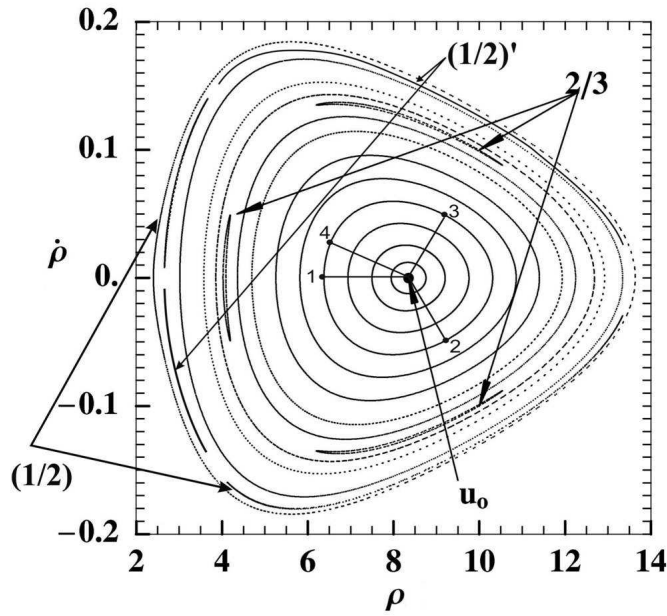


Fig. 4. The Poincaré surface of section ( $z = 0$ ) in the MN case containing orbits of the outer CZV.

of stability there are 4 points corresponding to 2 unstable periodic orbits of the resonance  $1/2$ , located at symmetrical positions with respect to the axis  $z = 0$ . Near the unstable periodic orbits the orbits are chaotic and their iterates on the Poincaré surface of section are scattered. In the case of Fig. 4 this scatter lies in extremely thin zones around and between the islands of stability. These zones are not visible in the figure.

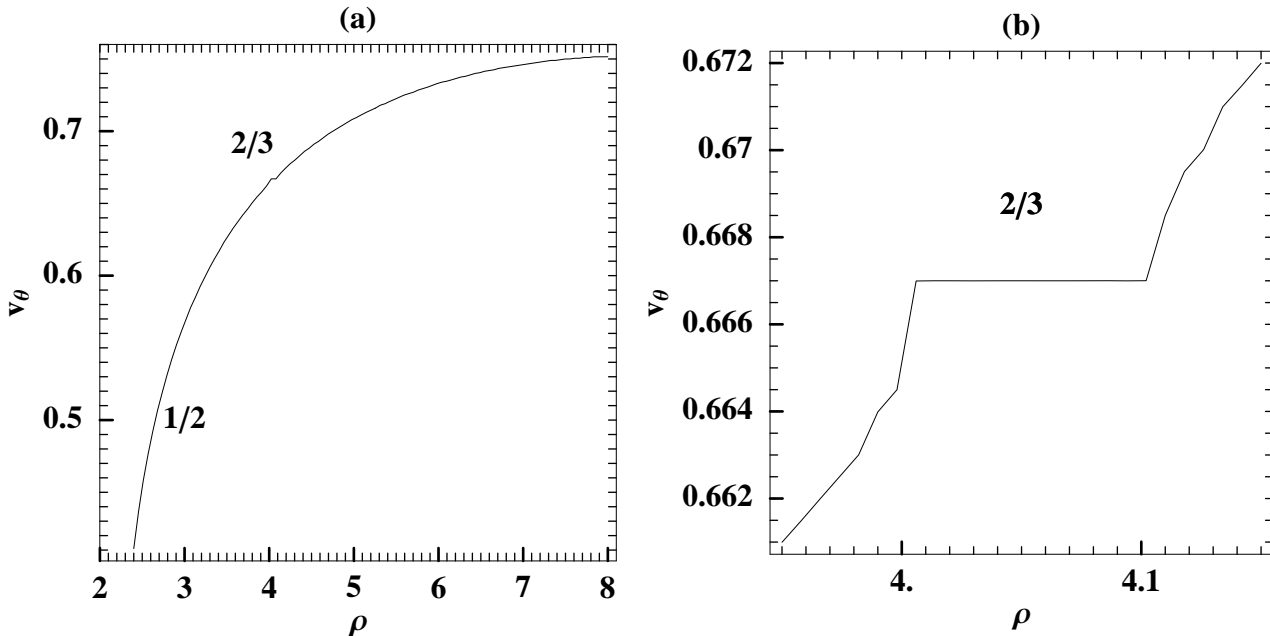


Fig. 5. (a) The rotation number  $\nu_\theta$  as a function of  $\rho$  along the line  $\dot{\rho} = 0$  (and  $z = 0, \dot{z} > 0$ ). (b) A magnification of the region close to the plateau at  $\nu_\theta = 2/3$ .

In order to find the islands of stability in Fig. 4 it is necessary to proceed along small steps in moving from one invariant curve to the next one. A systematic way to find the resonant islands and the respective chaotic domains is by calculating the rotation numbers along successive orbits at various distances from the central orbit  $\mathbf{u}_0$  (for a review see [Contopoulos, 2002]). Thus in Fig. 4 we have drawn the first 4 iterates of a regular orbit that has a rotation number larger than  $2/3$ . In order to measure the rotation number we compute the average fraction of a circle as we advance from one iterate to the next moving clockwise. The rotation number  $\nu_\theta$ , as a function of  $\rho$  along the axis  $\dot{\rho} = 0$  (on the surface of section at  $z = 0$ ) looks like a smooth monotonic curve (Fig. 5a). This is actually a smooth strictly monotonic curve in an integrable case, like the Kerr metric. However, in a nonintegrable case there are many (in fact infinite) plateaus near every resonant value (rational number), like the plateau of Fig. 5b. In order to find these plateaus we require a small step  $\Delta\rho$  between successive initial values of  $\rho$ . The orbits corresponding to the initial conditions of a plateau form a chain of islands around the stable resonant orbit, all with the same rotation number as the periodic orbit that lies at the centers of these islands, e.g. the orbits in the plateau  $2/3$  form 3 islands, all having the same rotation number  $2/3$ .

In an integrable case, like the Kerr metric, there are no islands of stability. All the resonant periodic orbits are neutrally stable and do not form islands around them. In fact a resonant invariant curve on which lies a periodic orbit of period  $T$  has all its points as initial conditions of periodic orbits with the same period  $T$ . Thus the existence of islands of stability is an indication of non-integrability. However, there are particular integrable systems with one type of islands of stability [Contopoulos, 1978], e.g. a Hamiltonian system of two degrees of freedom expressed in action angle variables which depends on the two actions  $J_1$ ,  $J_2$  and a particular combination of the angles  $n\theta_1 - m\theta_2$ , with  $n, m \in \mathbb{N}$ . Nonetheless a system with more than one type of islands (e.g. both double and triple islands in the same system) cannot be integrable. This is consistent with the non-existence of a Carter-type integral in generic non-Kerr cases [Flanagan & Hinderer, 2007; Brink, 2008]. However the outer permissible region of the MN system (the surface of section of which has been drawn in Fig. 4), is quite close to an integrable one. In this system chaos is very limited and thus not visible in Fig. 4. It exists mainly close to the unstable periodic orbits that lie between the islands of each chain of islands.

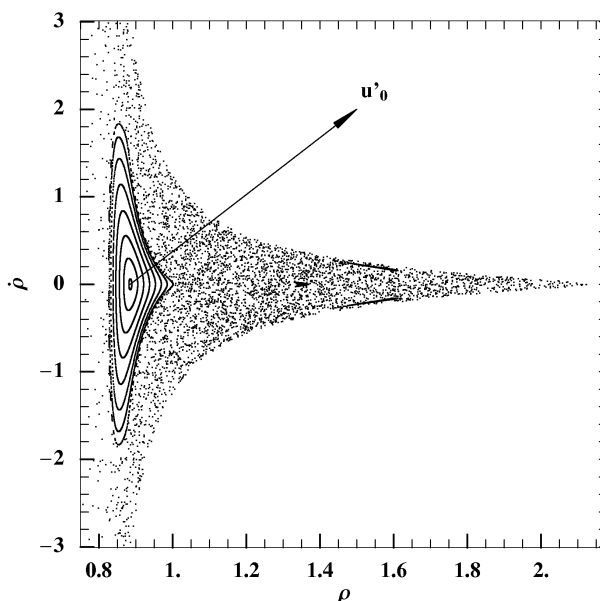


Fig. 6. The Poincaré surface of section of the inner permissible region in the case of Fig. 2a

On the other hand, the inner CZV (Fig. 2a) contains many chaotic orbits, but it contains also some

ordered orbits. On the Poincaré surface of section (Fig. 6) we see the chaotic domain and a large island of stability around a point  $\mathbf{u}'_0$ . There are also some very small islands of stability of multiplicity 3. The orbits in the inner regions of the MN system have not been studied in detail up to now and they have been considered “a very interesting puzzle” [Brink, 2008]. For this reason we study them in some detail in the present paper.

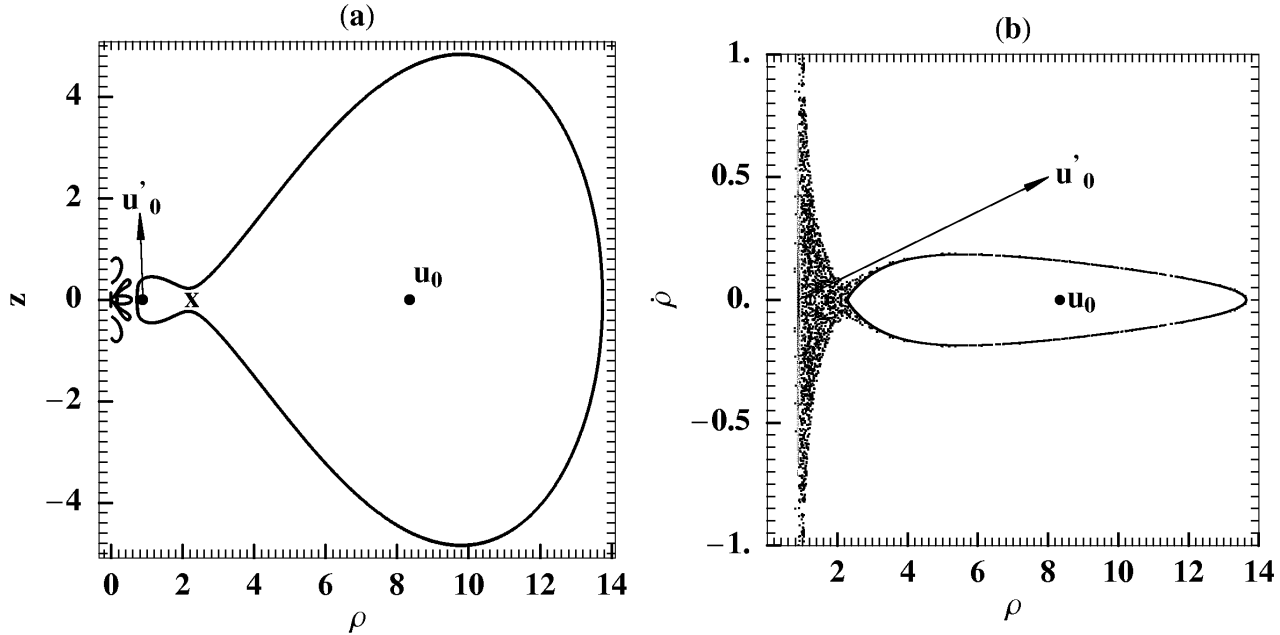


Fig. 7. (a) The CZVs on the  $(\rho, z)$  plane for  $E = 0.95$ ,  $L_z = 2.98$  and  $q = 0.95$ . The thick dots represent initial conditions (along with  $\dot{\rho}(0) = 0$ ) for stable periodic orbits while the “x” marks the initial condition of an unstable periodic orbit. (b) On the surface of section  $z = 0$  the chaotic domain of the inner permissible region expands and forms a chaotic layer just inside the boundary of the outer region.

If we decrease  $L_z$ , while keeping  $E$  and  $q$  fixed, the topology of the CZV changes (Fig. 7a). Namely for  $L_z = 2.98$ , just a little smaller from the value  $L_z = 3$  of Fig. 2a, the two main CZVs have joined. At the point of junction an unstable periodic orbit is formed between the two previously separate CZVs. This saddle point exists for  $L_z < 2.99761912$  and corresponds to the local maximum of the effective potential  $V_{\text{eff}}$  near  $\rho = 2$  (Fig. 2). On the corresponding Poincaré surface of section the permissible regions are joined; that is there are chaotic orbits that move in both regions. In this case the chaotic sea of the inner region has now been extended into the outer region as well, forming a chaotic layer around the whole ordered region which surrounds the point  $\mathbf{u}_0$  (Fig. 7b).

As  $L_z$  decreases further the neck joining the inner and the outer regions of the CZV, containing the non-plunging orbits, expands (Fig. 8a). Now the minimum  $\rho$  of the former CZV does not lie on the  $\rho$ -axis ( $z = 0$ ), as in Fig. 7a. In fact there are two minima with  $z \neq 0$ , at symmetrical locations with respect to the  $\rho$ -axis, which define the tips of two extensions of the CZV each approaching one of the two inner lobe-like CZVs which contain plunging orbits. These two CZVs lie on either side of the central lobe-like CZV which also contains plunging orbits. The permissible region of non-plunging orbits near these extensions contains mostly chaotic orbits (Fig. 8b).

For even lower values of  $L_z$  ( $L_z = 1.6$ ,  $E = 0.95$ ,  $q = 0.95$ ) the aforementioned extensions join the two symmetrical plunging areas around the central one (Fig. 9a) and all the chaotic orbits belonging to the chaotic sea, surrounding the island around the stable orbit  $\mathbf{u}_0$ , eventually plunge through the horizon. In Fig. 9a we observe the formation of another two symmetrical extensions of the main CZV for  $|z|$  values a little higher than for the already joined extensions. These extensions for still smaller  $L_z$  values ( $L_z = 1$ )



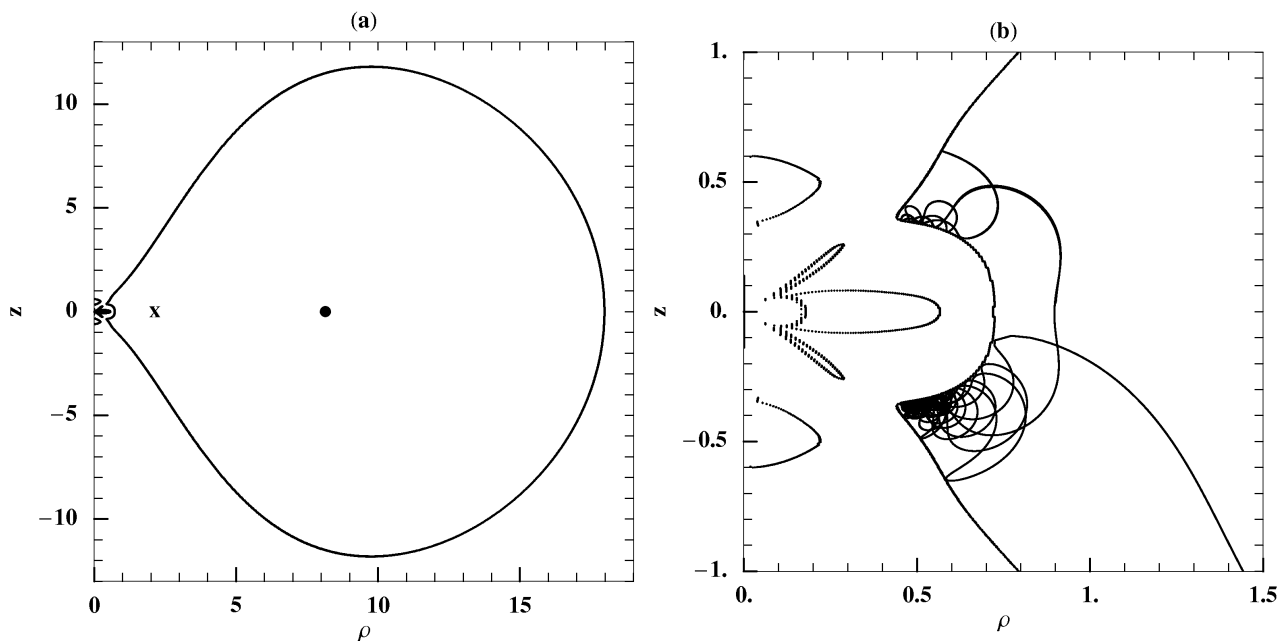


Fig. 8. (a) The CZVs for  $L_z = 1.7$ ,  $E = 0.95$ ,  $q = 0.95$ . The dot at the center of the diagram represents the initial condition for the stable orbit  $\mathbf{u}_0$  and the “x” represents the initial condition for the unstable periodic orbit. (b) A chaotic orbit in the inner part of the permissible space.

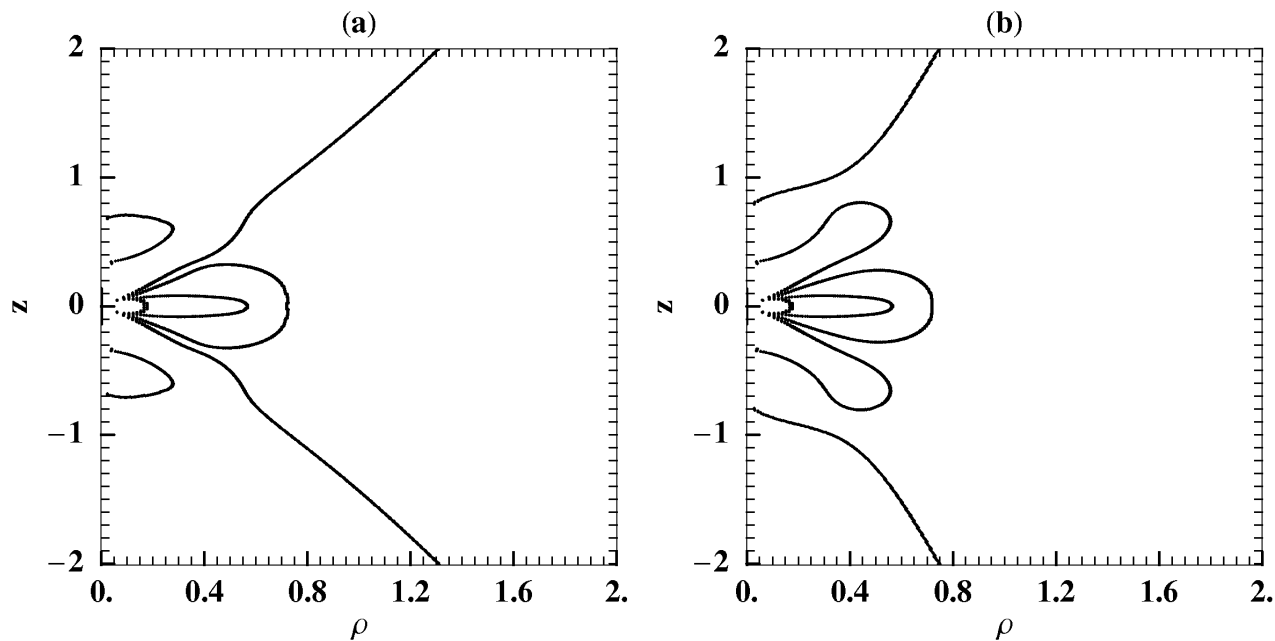


Fig. 9. (a) The CZVs for  $L_z = 1.6$ ,  $E = 0.95$ ,  $q = 0.95$  and (b) the CZVs for  $L_z = 1$ ,  $E = 0.95$ ,  $q = 0.95$  near the horizon  $\rho = 0$ .

join the two more distant plunging permissible areas (Fig. 9b) and create two more channels for chaotic orbits to plunge in.

While  $L_z$  decreases (with constant  $E = 0.95$  and  $q = 0.95$ ) the proportion of phase space surface occupied by the chaotic orbits on the surface of section  $z = 0$  increases. For  $L_z = 3$  most of the chaotic

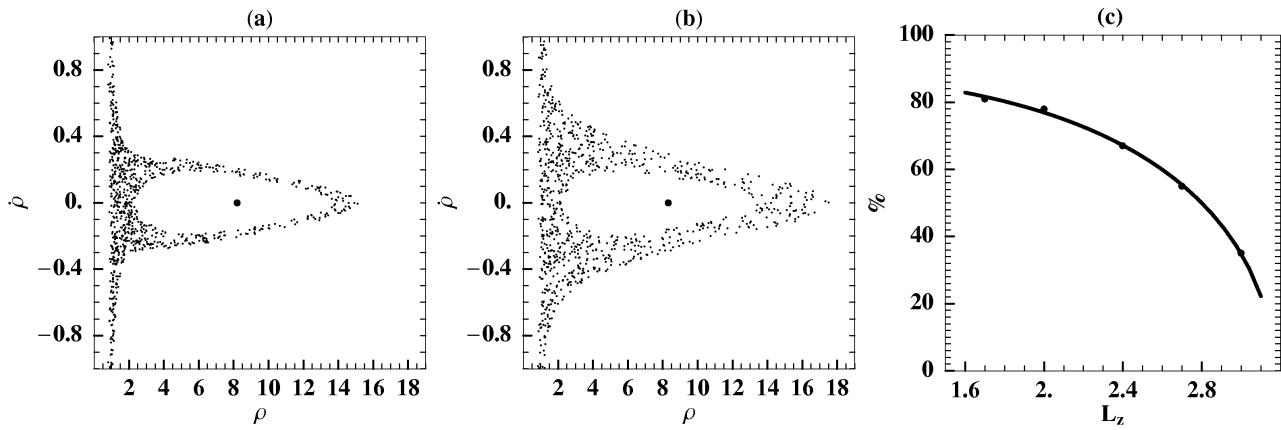


Fig. 10. Chaos on the Poincaré surfaces of section for (a)  $L_z = 2.7$  and (b)  $L_z = 1.7$ , surrounding a large region containing ordered orbits (the closed blank area). (c) The proportion of the available phase space covered by chaotic orbits as a function of  $L_z$  for  $E = 0.95$ ,  $q = 0.95$ .

orbits are inside the inner closed CZV, but this region contains also an important island of stability (see Fig. 6). There are also very small regions of chaos around the unstable periodic orbits of the outer permissible region. The proportion of the area on the surface of section  $z=0$  that is occupied by chaotic orbits is about 20%. In order to estimate this fraction, we measured the area occupied by the chaotic orbits on the surface of section and we divided it by the total area covered by the allowed orbits. At lower values of  $L_z$ , the inner island of stability (around  $\mathbf{u}'_0$ ) shrinks in size, and chaos starts occupying the envelope of the ordered region in the outer part of the now joined permissible region (Fig. 7b). The proportion of the total area on the surface of section  $z = 0$  occupied by chaotic orbits as a function of  $L_z$  is given in Fig. 10c. We see that the proportion of chaotic orbits increases as  $L_z$  decreases (Figs. 10a,b), and for  $L_z \leq 1.6$  it is already larger than 80%.

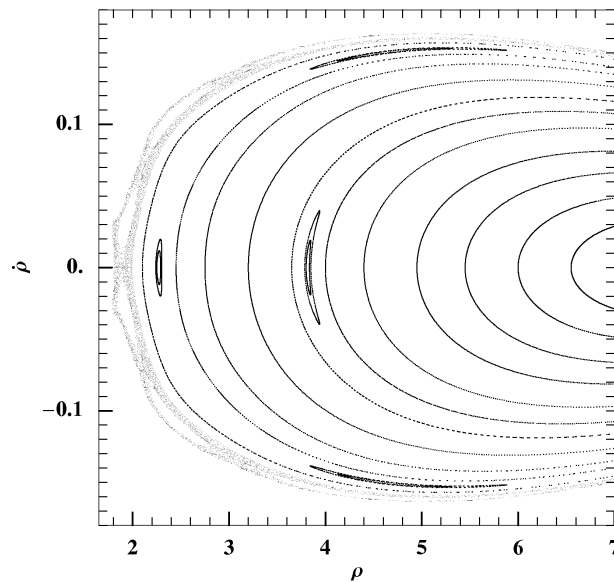


Fig. 11. A sticky chaotic domain (dark ribbon with holes) surrounding the region of ordered orbits for  $L_z = 0.1$ ,  $E = 0.95$ ,  $q = 0.95$ . In the ordered region there are islands of stability of the resonances  $1/3$  and  $1/2$ . The sticky zone contains also several higher order islands of stability.

For even smaller values of  $L_z$  ( $L_z \lesssim 1.6$ ) all the chaotic orbits belonging to the chaotic sea surrounding the main island of stability plunge through the horizon, while the chaotic orbits which appear between the islands inside the main island remain non-plunging. On the other hand orbits just outside the boundary of the main island stay there for a long time before they plunge in. These orbits that stay close to the boundary of the main island exhibit stickiness (for a review about stickiness see [Contopoulos, 2002]). In Fig. 11 we see this sticky domain as a dark ribbon with small empty holes. The empty holes contain higher order islands of stability. Orbits starting on the left of the dark ribbon of Fig. 11 plunge in through the horizon very fast and do not produce the densely populated chaotic regions as in Figs. 10a,b.

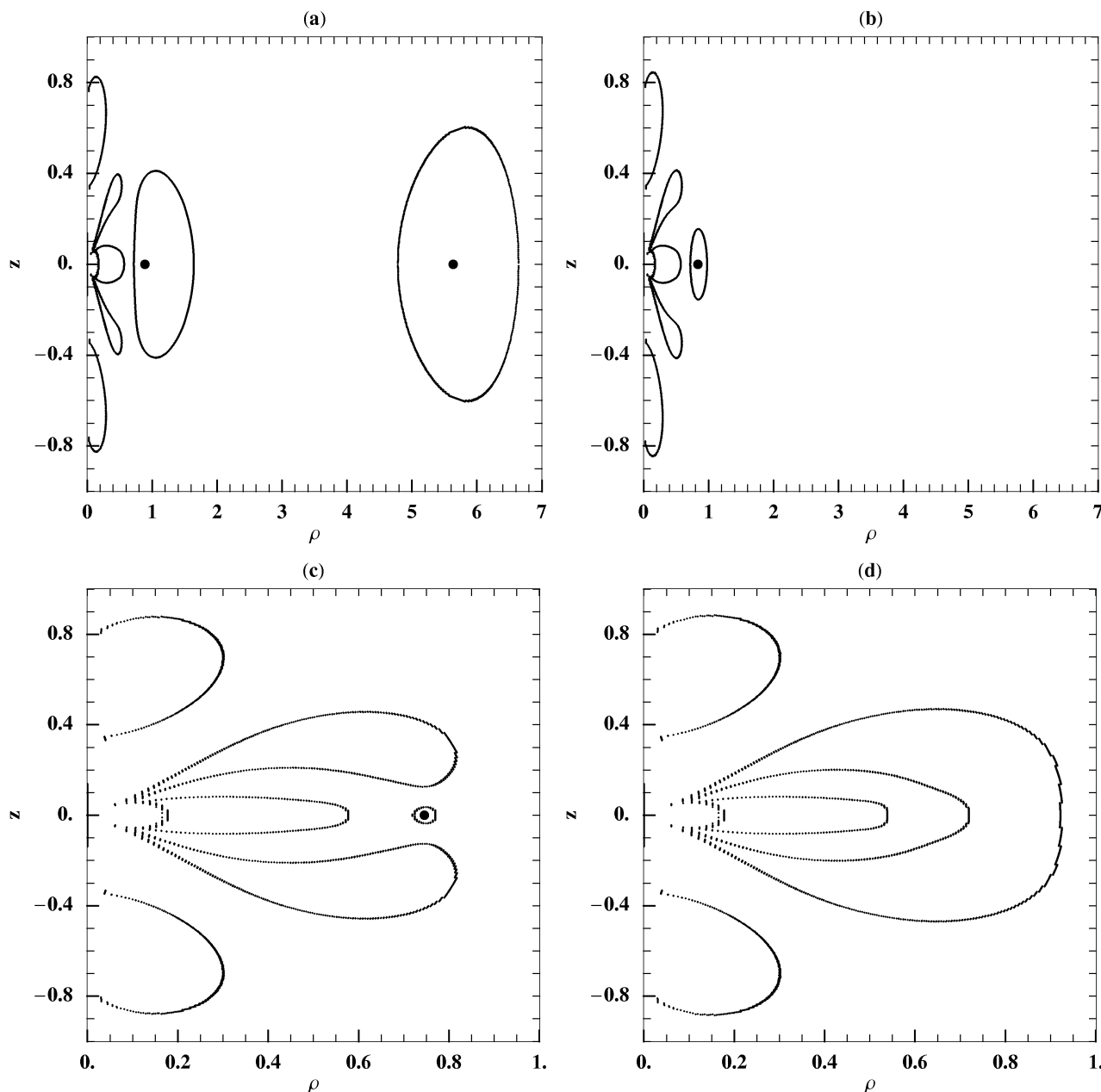


Fig. 12. The CZVs for (a)  $E = 0.935$ , (b)  $E = 0.7$ , (c)  $E = 0.2$  and (d)  $E = 0.1$  while  $L_z = 3$ ,  $q = 0.95$ .

Next we consider the orbits for low values of  $E$ . In order to study them we first examine how the shape of the CZVs changes if we keep  $L_z$  and  $q$  constant ( $L_z = 3$ ,  $q = 0.95$ ), but decrease the energy. What we get is the series of curves of Fig. 12. As  $E$  decreases below  $E = 0.95$  the two permissible regions of non-plunging orbits get further and further apart and they shrink. For  $E \approx 0.93210$  the outer region disappears and for even smaller  $E$ , there is only one permissible region with non-plunging orbits, the one that was previously called the inner region. This region shrinks further as  $E$  decreases (compare Fig. 12a corresponding to  $E = 0.935$  and Fig. 12b corresponding to  $E = 0.7$ ) and for  $E = 0.2$  it is restricted between the three central CZVs of plunging orbits (Fig. 12c). For even smaller  $E$  the two CZVs of plunging orbits, above and below the equatorial plane join. When this happens most orbits plunge fast through the horizon (Fig. 12d).

The details of the transition from Fig. 12c to 12d are of particular interest. The non plunging region of Fig. 12c for  $E = 0.2$  consists almost exclusively of ordered orbits, which are shown in Fig. 13a. The orbits are deployed around a central periodic orbit  $\mathbf{u}'_0$  at  $\rho \approx 0.745$ . As  $E$  decreases the periodic orbit moves closer to the horizon, and for  $E = 0.192$  it is at  $\rho \approx 0.736$  (Fig. 13b). In Fig. 13b we see also another stable periodic orbit (point  $\mathbf{u}''_0$ ) at  $\rho \approx 0.764$  and an unstable periodic orbit at  $\rho \approx 0.775$  (point  $\mathbf{u}'''_0$ ). The latter pair of orbits was first formed at  $E \simeq 0.193$  at a ‘‘tangent bifurcation’’ (these orbits bifurcate only from each other). Most orbits in Fig. 13b are ordered and form closed invariant curves. In particular the invariant curves close to the boundary surround both islands around  $\mathbf{u}'_0$  and  $\mathbf{u}''_0$ . There is only a very small chaotic region close to the unstable point  $\mathbf{u}'''_0$  and its asymptotic curves.

As  $E$  increases further the chaotic region around the unstable point  $\mathbf{u}'''_0$  swells and diffuses towards the boundary of the islands (Fig. 13c). At particular values of  $E$  we have bifurcations of higher order periodic orbits from the central point  $\mathbf{u}''_0$ . E.g. in Fig. 13c (corresponding to  $E = 0.191$ ) we see a double island with rotation number  $\nu_\theta = 1/2$  and a triple island with rotation number  $\nu_\theta = 1/3$ .

For  $E = 0.1903$  (Fig. 13d) chaos has increased considerably and we see further bifurcating islands around  $\mathbf{u}''_0$  (now at  $\rho \approx 0.760$ ). In particular we see 2 islands with rotation number  $\nu_\theta = 1$  ( $\rho \approx 0.756$  and  $\rho \approx 0.765$ ); these two islands consist of two distinct orbits, in contrast to what happens when  $\nu_\theta = 1/2$  where an orbit starting at one island passes alternatively through both islands.

When  $E < 0.1901$  the lobes of the curves of zero velocity above and below the region of the non-plunging region of Fig. 12c join the central non-plunging region. Then most of the chaotic orbits escape upwards or downwards along the  $z$ -axis, and finally plunge through the horizon (see Fig. 14a which corresponds to  $E = 0.1899$ ). However, an island of stability still remains around  $\rho = 0.73$  (Fig. 14b). As  $E$  decreases further the stable periodic orbit  $\mathbf{u}'_0$  moves further inwards, very close to the inner boundary. For  $E < 0.1858$   $\mathbf{u}'_0$  becomes unstable and for a little smaller  $E$  the island around it disappears. On the other hand the island generated around  $\mathbf{u}''_0$  persists for  $E = 0.18$  but for  $E = 0.17$  it has disappeared.

It is remarkable that the inner permissible region of the non-plunging orbits assumes its smallest size for  $E \approx 0.265$ , below which it starts expanding again before it gets swallowed by the lobes of the plunging regions.

### 3. Characteristics

The position of a periodic orbit as a function of a parameter of the system is called a characteristic. In Fig. 15 we give the characteristics of the main families of periodic orbits in the MN metric (for  $q = 0.95$ ,  $\chi = 0.9$ ), namely the central periodic orbit of the outer region (the ‘‘main island center’’  $\mathbf{u}_0$ ), the periodic orbit  $2/3$  (the point lying on the line  $\dot{\rho} = 0$  of the surface of section at  $z = 0$ ), and the unstable saddle orbit, as functions of  $L_z$  for  $E = 0.95$  (Fig. 15a) and as functions of  $E$  for  $L_z = 3$  (Fig. 15b). In the same figures we have drawn also the boundaries of the permissible regions for  $z = 0$ , i.e. the intersections of the CZVs with the axis  $z = 0$ . These are the outer and the inner boundaries of the non-plunging orbits region, when the non-plunging regions are joined. When there are two distinct regions containing non-plunging orbits we mark the middle outer boundary (MOB), that is the inner boundary of the outer region, and the middle inner boundary (MIB), that is outer boundary of the inner region.

In Fig. 15a we see that the central orbit ( $\mathbf{u}_0$ ) has an almost constant position, while the orbit  $2/3$  bifurcates from the central family for  $L_z \approx 0.75$  and moves inwards (towards  $\rho = 0$ ) as  $L_z$  increases. This

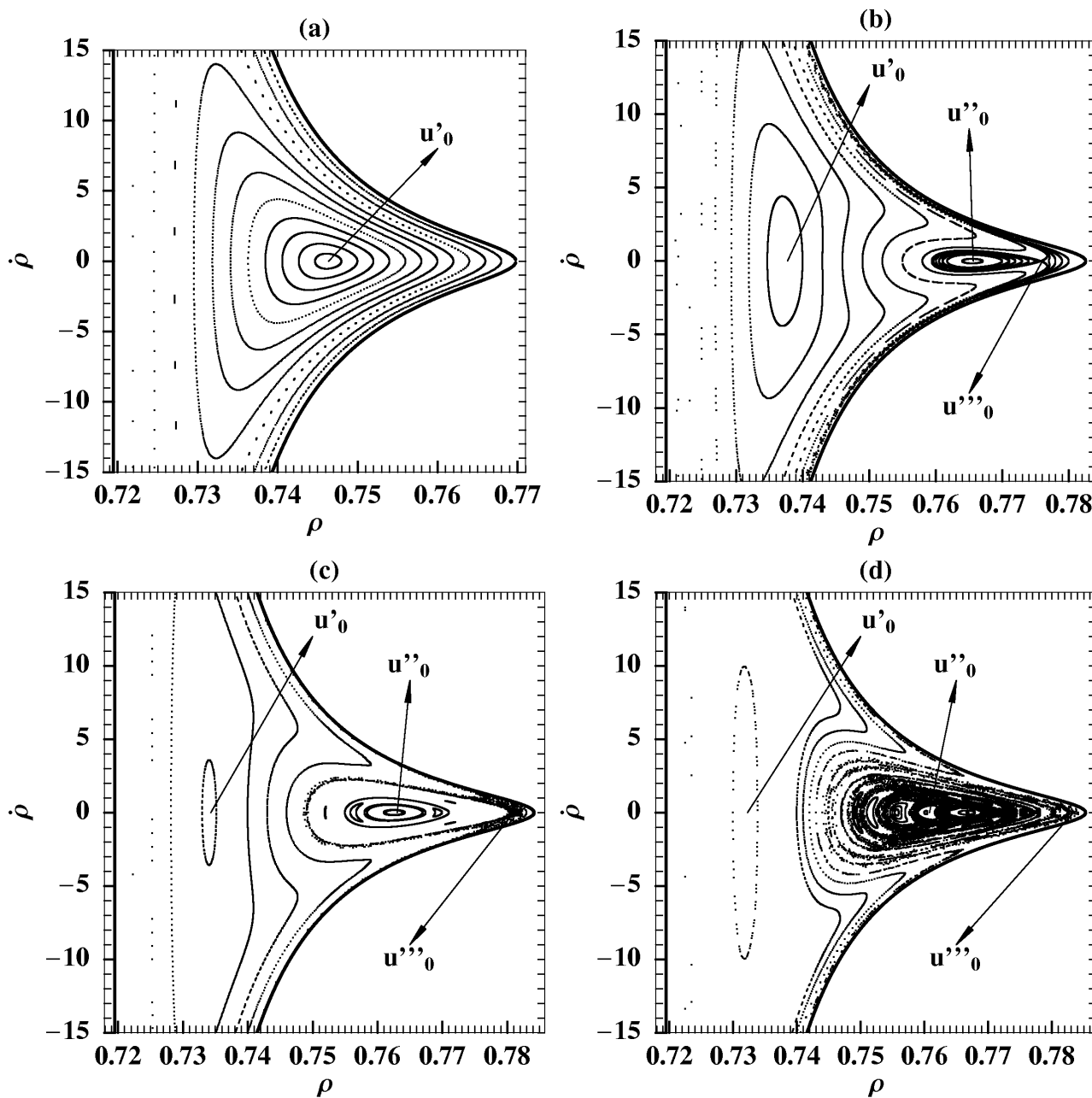


Fig. 13. Invariant curves and chaos on the surface of section  $(\rho, \dot{\rho}, z = 0)$  for (a)  $E = 0.2$ , (b)  $E = 0.192$ , (c)  $E = 0.191$  and (d)  $E = 0.1903$  (with  $L_z = 3, q = 0.95$ ).

orbit reaches the MOB for  $L_z \approx 3.15$  while for larger  $L_z$   $\mathbf{u}_0$  does not exist at all. The saddle point is generated when the two non-plunging CZVs merge for  $L_z = 2.99762$  and then it moves inwards as  $L_z$  decreases. On the other hand the outer boundary of the outer CZV moves to large distances when  $L_z$  decreases, while the corresponding inner boundary remains at a constant distance from the horizon. The MOB and the MIB show up for  $L_z \geq 2.99762$ . For larger  $L_z$  the MIB and the MOB get further apart, i.e. the MIB moves inwards while the MOB moves outwards. For  $L_z \approx 3.40935$  the outer boundary and the MOB join, and then the outer region completely disappears. On the other hand the MIB moves inwards as  $L_z$  increases and appears to level off for  $L_z > 3.4$ .

In Fig. 15b we give the characteristics and boundaries as functions of  $E$ . As  $E$  increases, the outer

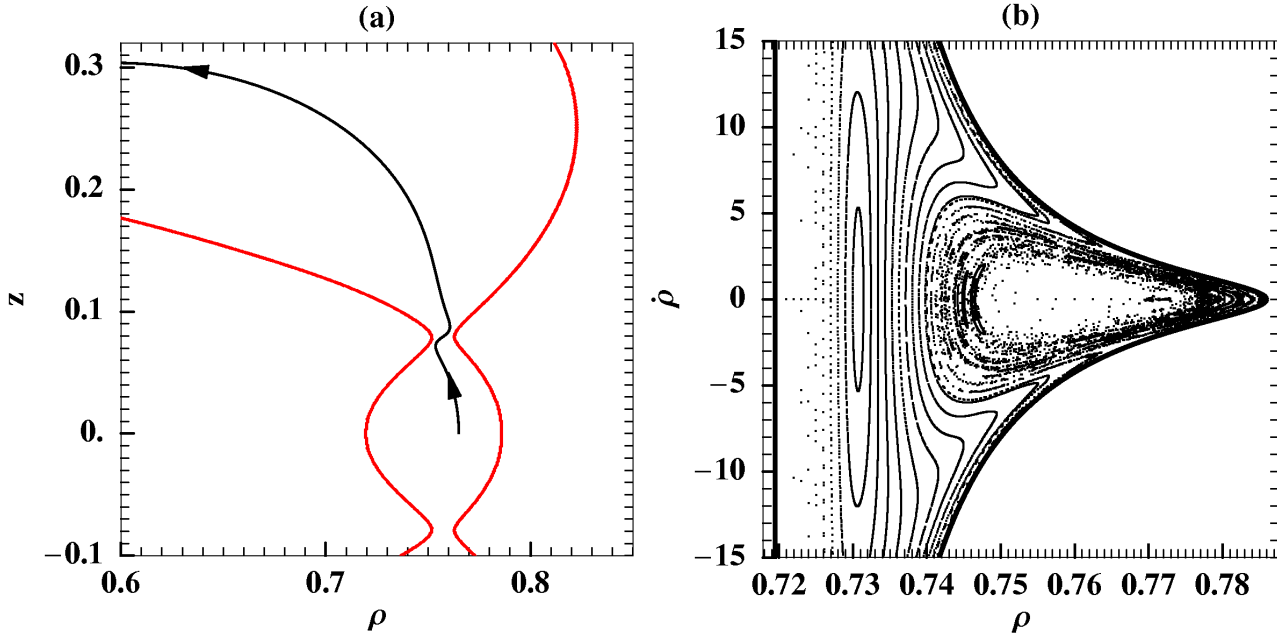


Fig. 14. (a) An orbit escaping upwards ( $z > 0$ ) and plunging through the horizon for  $E = 0.1899$  ( $L_z = 3, q = 0.95$ ). (b) The corresponding surface of section. There is a large island surrounding  $\mathbf{u}_0'$  (near  $\rho = 0.7308, \dot{\rho} = 0$ ), some islands of higher order on the right part of the figure, and an almost blank region of the fast escaping orbits, surrounded by chaotic orbits that escape after a larger time.

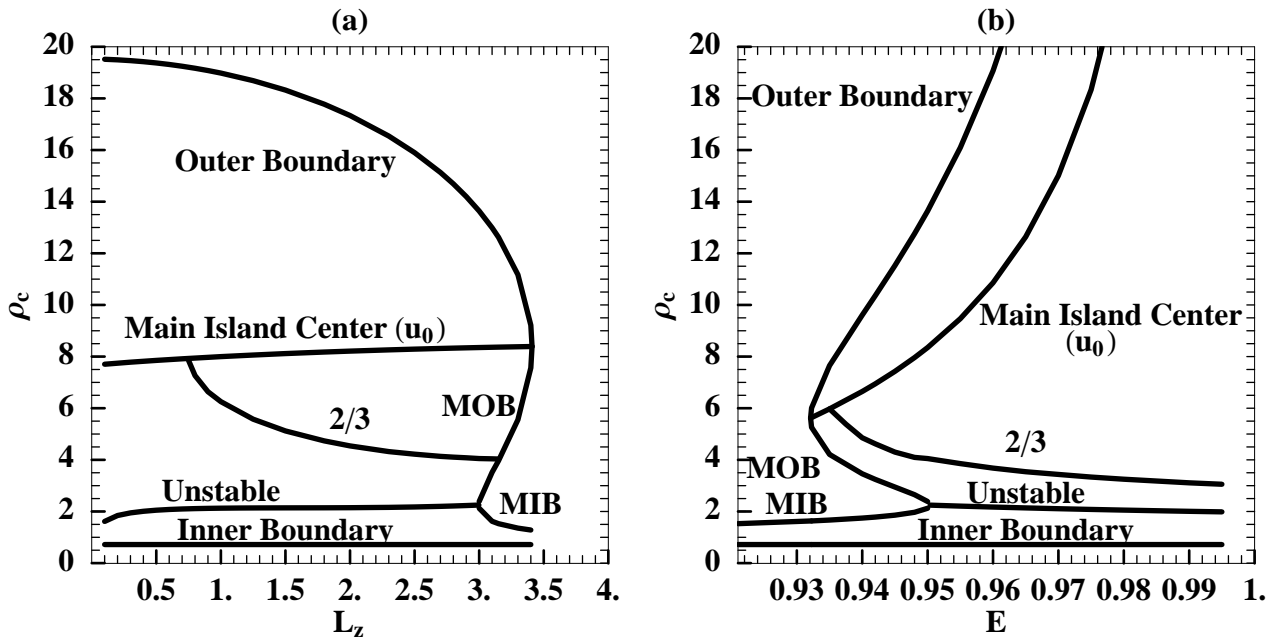


Fig. 15. The characteristics of the main families of periodic orbits (for  $q = 0.95, \chi = 0.9$ ) in the MN metric along the line  $\rho$  on the surface of section at  $z = 0$  and the corresponding boundaries of the permissible regions (a) as functions of  $L_z$  for  $E = 0.95$ , and (b) as functions of  $E$  for  $L_z = 3$ .

boundary increases enormously, approaching infinity as  $E \rightarrow 1$ , while the inner boundary remains at an almost constant position. The central periodic orbit ( $\mathbf{u}_0$ ) moves also outwards for increasing  $E$ , while the

orbit 2/3 moves inwards. The orbit 2/3 bifurcates from the central orbit for  $E \approx 0.935$ . For large  $E$  we have a unique large CZV containing the non plunging orbits, but for  $E \leq 0.95038$  the permissible region splits into two. The inner region is between the MIB and the inner boundary. This region shrinks slightly as  $E$  decreases. The outer region is between the MOB and the outer boundary. This region shrinks quickly as  $E$  decreases and finally at  $E \approx 0.93210$  it disappears. For  $E \leq 0.93210$  there is no outer region and thus no central periodic orbit  $\mathbf{u}_0$ . As long as the CZV is unique ( $E \geq 0.95038$ ) there is also an unstable saddle point which moves slightly inwards as  $E$  increases.

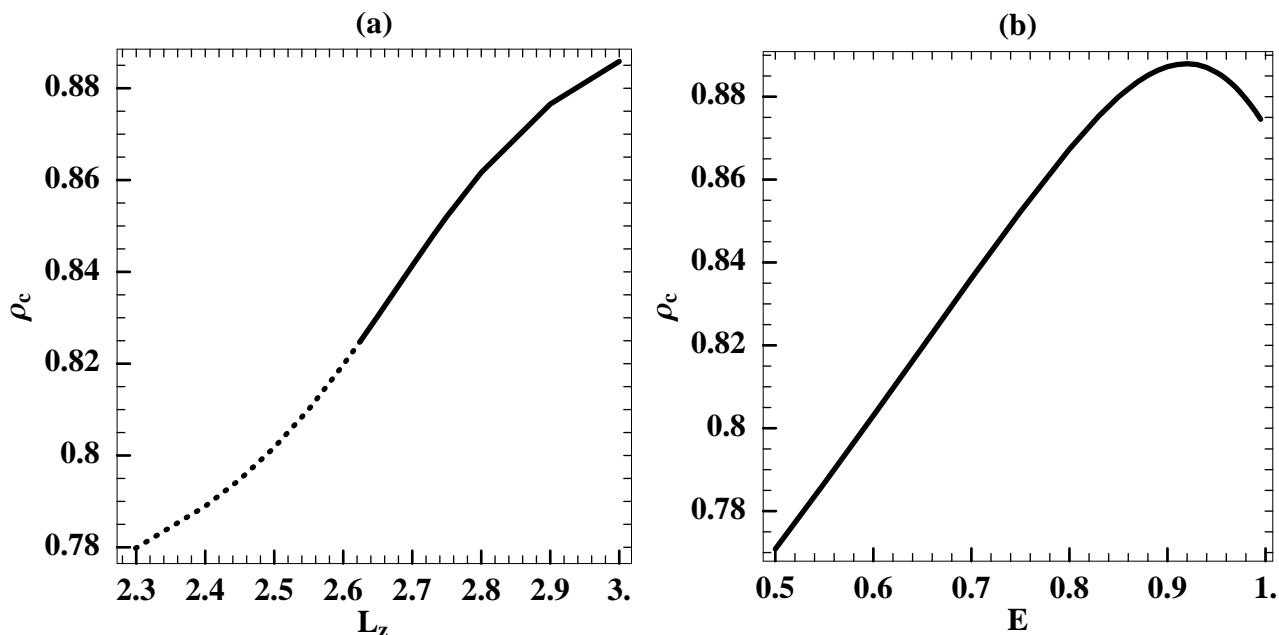


Fig. 16. The characteristic of the periodic orbit  $\mathbf{u}'_0$  lying in the center of the main island of the inner region (for  $q = 0.95$ ,  $\chi = 0.9$ ) (a) as function of  $L_z$  for  $E = 0.95$  and (b) as function of  $E$  for  $L_z = 3$ . The dotted lower part of the curve of Fig. 16a indicates that the periodic orbit has become unstable.

The characteristics of the stable periodic orbit  $\mathbf{u}'_0$  of the inner region as functions of  $L_z$  and  $E$  are shown in Fig. 16. The periodic orbit  $\mathbf{u}'_0$  is very close to the inner boundary shown in Fig. 15. For  $E = 0.95$  and  $L_z > 2.6125$ ,  $\mathbf{u}'_0$  is stable, but for  $L_z < 2.6125$  it becomes unstable. On the other hand as we decrease  $E$  for constant  $L_z = 3$ , the periodic orbit  $\mathbf{u}'_0$  moves initially (as long as  $E \gtrsim 0.92$ ) outwards (see Fig. 16b), but for  $E \lesssim 0.92$ ,  $\mathbf{u}'_0$  moves inwards, until it reaches a minimum value for  $E \approx 0.265$ . For the interval  $0.265 \gtrsim E \gtrsim 0.196$  the point  $\mathbf{u}'_0$  moves slightly outwards for decreasing  $E$ , and then for  $E \lesssim 0.196$ ,  $\mathbf{u}'_0$  moves inwards again (Fig. 17). The size of the region of permissible motion decreases as  $E$  decreases (Fig. 12a,b), but for  $E \lesssim 0.265$  this region starts expanding again.

The details of the characteristics of the periodic orbits for  $E \leq 0.2$  are shown in Fig. 17. We see the characteristic of the main periodic orbit  $\mathbf{u}'_0$  of the inner island and the boundary of the permissible region along the line  $z = 0$ . Furthermore we have drawn the characteristics of the periodic orbits  $\mathbf{u}''_0$  and  $\mathbf{u}'''_0$  of Fig. 13, and of the main bifurcating families from  $\mathbf{u}'_0$  along the axis  $\dot{\rho} = 0$ . The rotation number along every family bifurcating from  $\mathbf{u}'_0$  is constant and it is marked in Fig. 17. The rotation number of the orbit  $\mathbf{u}'_0$  (the limit of the rotation number of the invariant curves around  $\mathbf{u}'_0$  as they shrink to  $\mathbf{u}'_0$ ) increases as  $E$  decreases. When the rotation number  $\nu_\theta$  of  $\mathbf{u}'_0$  becomes  $\nu_\theta = 1/2$  the orbit  $\mathbf{u}'_0$  becomes unstable and a stable family  $1/2$  bifurcates. For a small interval of values  $\Delta E$  of decreasing  $E$ ,  $\mathbf{u}'_0$  remains unstable, and for even smaller  $E$  it becomes stable again. When  $\nu_\theta = 1$  the orbit  $\mathbf{u}'_0$  generates by bifurcation a stable family  $1/1$  and becomes again unstable. For smaller  $E$  the family  $\mathbf{u}'_0$  has an infinity of transitions to stability and instability. The phenomenon of infinite transitions to instability and stability that leads

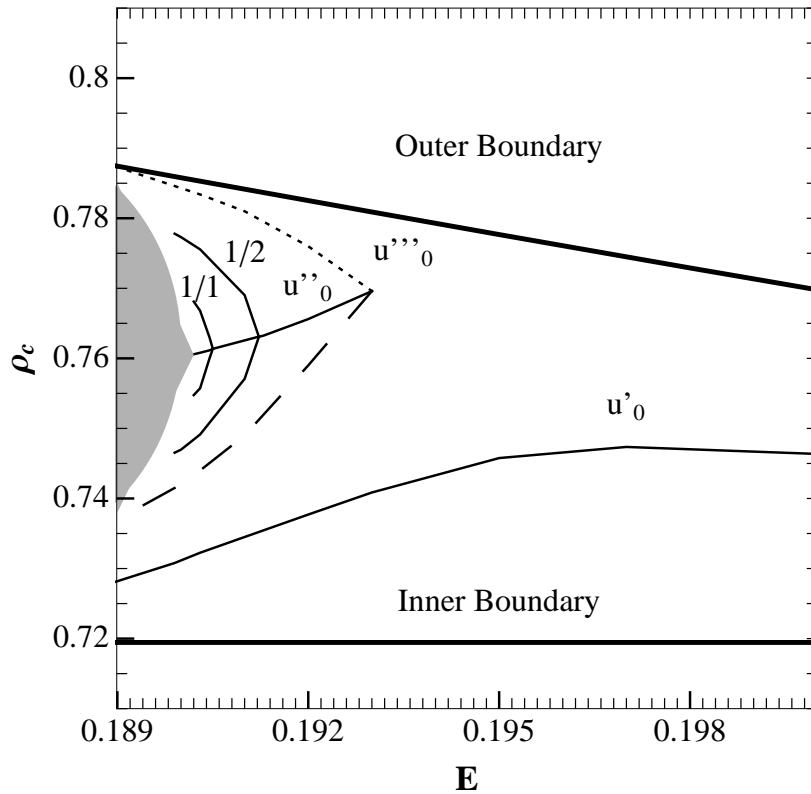


Fig. 17. Characteristics of the periodic orbits and boundaries of the inner region for  $0.189 < E < 0.2$ . Stable orbits are denoted with continuous lines, and unstable orbits with dotted lines. The unstable intervals of  $\mathbf{u}''_0$  on the left of the bifurcating families  $1/2$  and  $1/1$  are very small and they are not marked. The gray area for  $E \leq 0.1901$  represents chaotic orbits plunging through the horizon. The asymptotic curves of the unstable orbit  $\mathbf{u}''_0$  intersect at the first homoclinic points along the dashed curve. Close to this curve and to the curve  $\mathbf{u}''_0$  the orbits are chaotic.

to the termination of a family of periodic orbits at the escape energy was described in detail in a different dynamical system [Contopoulos & Zikides, 1980; Contopoulos et al., 1987]. In the present case when  $E$  tends to 0.1901 the period of the orbit  $\mathbf{u}''_0$  should tend to infinity and for  $E \leq 0.1901$ , when the CZVs have opened, the periodic orbit  $\mathbf{u}''_0$  should not exist anymore. The orbits close to  $\mathbf{u}''_0$  escape and plunge through the horizon as shown in Fig. 14a. The region of escaping orbits is shown in Fig. 17 with gray color. We notice that this region increases abruptly as  $E$  decreases below the escape energy  $E = 0.1901$ .

In Fig. 17 we have marked the characteristic of the unstable family  $\mathbf{u}''_0$  (dotted line) and the locus of the first homoclinic intersection of the asymptotic curves of the orbit  $\mathbf{u}''_0$  (dashed line). The characteristic of  $\mathbf{u}''_0$  approaches the outer boundary as  $E$  decreases. Close to these lines the orbits are chaotic. However chaos is quite limited for  $E$  only slightly smaller than its value at the tangent bifurcation of the orbits  $\mathbf{u}''_0$  and  $\mathbf{u}''_0$  (e.g. for  $E = 0.192$ , Fig. 13b). The asymptotic curves from the unstable orbit  $\mathbf{u}''_0$  separate the invariant curves that close around  $\mathbf{u}''_0$  from those that close around  $\mathbf{u}'_0$  (Fig. 13b). As  $E$  decreases chaos becomes more important (Figs. 13c,d), and when  $E$  is smaller than the escaping energy (the energy at which the closed CZV of (Fig. 13c) join the upper and lower CZVs of the plunging orbits) most chaotic orbits escape.

The family  $\mathbf{u}'_0$  remains stable as  $E$  decreases to the left of the border of Fig. 17, until  $E \approx 0.186$ . For a little smaller  $E$  this family becomes unstable and for even smaller  $E$  the surrounding invariant curves disappear. On the other hand the island formed by the invariant curves around  $\mathbf{u}''_0$  continues to exist, even when this orbit and the nearby orbits escape, but for  $E \lesssim 0.17$  almost all orbits escape.



#### 4. Nongeodesic orbits

In real EMRI systems the energy and the angular momentum are not conserved; they change adiabatically due to gravitational radiation. Thus the real orbits are nongeodesic, although their deviation from geodesics is very small. An estimate of the loss of energy and angular momentum per unit time for a test body in Kerr metric,  $\frac{dE}{dt}$  and  $\frac{dL_z}{dt}$ , has been provided by [Gair & Glampedakis, 2006] (see Eqs. (44,45)). We use these formulae, appropriately modified, to compute approximately the corresponding losses in our MN system [Gair et al., 2008; Lukes-Gerakopoulos et al., 2010].

For a relatively small time interval we may consider  $\frac{dE}{dt}$  and  $\frac{dL_z}{dt}$  almost constant; thus

$$E = E_0 + \frac{dE_0}{dt} t, \quad L_z = L_{z0} + \frac{dL_{z0}}{dt} t \quad (4)$$

where  $E_0, L_{z0}$  are the corresponding initial values and  $\frac{dE_0}{dt}, \frac{dL_{z0}}{dt}$  are negative, and represent the constant rates of loss. The rates of loss depend on the mass ratio of the EMRI system; in fact as this ratio tends to 0 the motion tends to become more and more geodesic.

We have applied these approximate formulae in our numerical calculation of the orbits for several orbital periods. During this time the structure of the phase space changes gradually, e.g. the location and the size of the resonant islands change. If an orbit starts away from the main resonant islands it moves adiabatically along different invariant curves and, as a consequence, its rotation number gradually changes in an apparently strictly monotonic way. But if the orbit passes through an island of stability its rotation number remains constant and equal to a fixed rational number, like  $2/3$ .

In the corresponding integrable case (the Kerr metric), there are no islands of stability, thus the variation of the rotation number  $\nu_\theta$  is always strictly monotonic in time. However, in a non-integrable non-Kerr metric (like the MN metric) there are several islands of stability and an orbit passing through them assumes a constant value of  $\nu_\theta$  for some interval of time. In this interval the rotation curve exhibits a corresponding plateau. The existence of such plateaus can be used as an observational criterion to distinguish a Kerr from a non-Kerr background, since the rotation number can be inferred from the spectrum of the gravitational waves.

In Fig. 18a we show a non geodesic orbit for an interval of time during which the orbit crosses the resonance  $2/3$ . Initially the non geodesic orbit is outside but close to the island of stability  $2/3$  and its initial condition lies in the area between the  $2/3$  resonance and the central orbit  $\mathbf{u}_0$ . The angles formed between the successive intersections of the non geodesic orbit on the surface of section at  $z = 0$  as they are seen from the central periodic orbit  $\mathbf{u}_0$  are slightly larger than  $4\pi/3$ . Thus third intersection lies approximately at a particular invariant curve with  $\nu_\theta > 2/3$ . In Fig. 18a we have joined every third intersection by a continuous line. Thus the non geodesic curve crosses successive invariant curves and revolves around  $\mathbf{u}_0$ . When these intersections enter the  $2/3$  resonance, e.g. the leftmost island of the 3 islands (Fig. 4), they tend to follow the circulation of the geodesic orbits, corresponding to the instantaneous values of  $E$  and  $L_z$ , that form the island itself. As time progresses and  $E, L_z$  change, these resonance islands move gradually closer to  $\mathbf{u}_0$ , e.g. the leftmost island moves to the right. The non geodesic orbit follows the drift of the island while it moves around the island for some time. If the time it remains inside the island is sufficient, each third intersection of the non geodesic orbit may form a number of loops. In Fig. 18a they form 2 loops inside the leftmost island. Later on these intersections exit the island and then form a curve which approximates invariant curves around the central orbit  $\mathbf{u}_0$  with rotation number  $\nu_\theta < 2/3$ . Because of the previously described relative ‘‘motion’’ of the non geodesic orbit and the geodesic background, a non geodesic orbit whose initial condition lies between the  $2/3$  resonance and the orbit  $\mathbf{u}_0$  will eventually cross the  $2/3$  resonance and will finally find itself on the other side of the resonance island.

The corresponding fundamental frequencies of the spectrum of the gravitational radiation change in time and their ratio follows a curve like the one in Fig. 18b. When the non geodesic orbit is outside the resonance ( $\nu_\theta > 2/3$ ) the value of  $\nu_\theta$  appears to decrease strictly monotonically. When the non geodesic orbit is entrapped inside the resonance its rotation number remains theoretically constant. After the non geodesic orbit exits the resonant region the rotation number appears to decrease again strictly monotonically. (For a more detailed discussion of the relation between the fundamental frequencies of the spectrum and  $\nu_\theta$  see [Lukes-Gerakopoulos et al., 2010].)

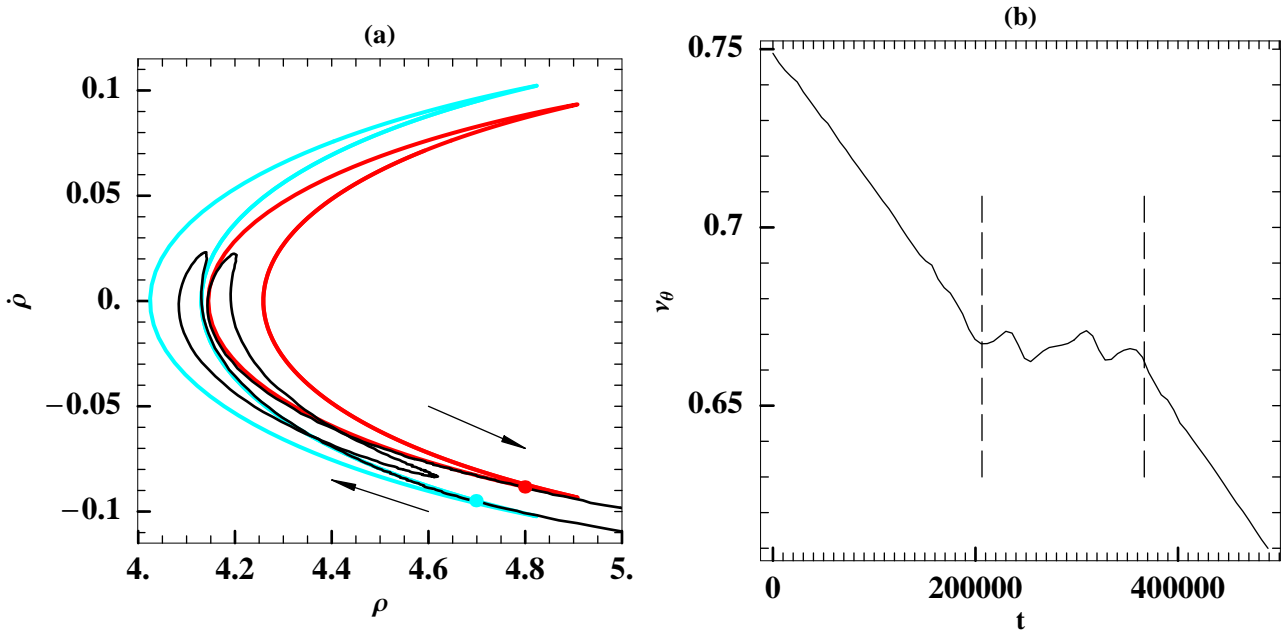


Fig. 18. (a) The black line joins the third intersections of a non geodesic orbit ( $z = 0$ ) and passes through an island of stability of the  $2/3$  resonance. This black line performs a couple of windings on a surface of section while the non geodesic loses energy and angular momentum due to gravitational radiation. The blue point indicates the point of entrance of the nongeodesic orbit to the resonance, while the red indicates the exit. The blue and the red curves represent the geodesic orbits if the blue point and the red point are used as an initial conditions. (b) The evolution of the ratio of the corresponding fundamental frequencies as a function of time for the orbit in (a). The dashed lines show the time interval during which the non geodesic orbit is trapped. The present evolution of the non geodesic orbit corresponds to a binary with ratio of masses equal to  $8 \times 10^{-5}$ .

In Fig. 4b we see small oscillations of  $\nu_\theta$  during the trapping period. This is due to the finite time for which we evaluate the frequencies during the evolution of the non geodesic loops. We cannot evaluate the frequencies for larger time intervals, because the frequencies change continuously, although this change is very slow. This imposed finiteness in the frequency analysis has a side effect: the loops are not averaged and therefore an extra illusive frequency -the one connected with the circulation of the island-appears.

## 5. Conclusions

In this paper we have studied thoroughly the details of the various types of orbits in a MN spacetime. The non-integrability of the corresponding geodesic equations is quite clear since all the general characteristics exhibited by systems that deviate from an integrable one are present in this case as well. Namely, more than one chains of Birkhoff islands are present in a surface of section, while chaotic regions are also present. The most important chaotic region is mainly present in the inner closed CZV, where the deviation from the Kerr metric is more pronounced. Also when the two regions of allowed orbits are joined, the chaotic behavior of the inner region is partly transferred in the outer region. We have also examined the behavior of the regions containing non plunging orbits when the parameters of the system (mainly  $E$ ,  $L_z$ ) change, and take extreme values.

Finally we studied the case of a non geodesic orbit as it moves adiabatically in and out of a resonance island. The plateau in the evolution of the ratio of the corresponding gravitational wave signal frequencies, that was analyzed in [Lukes-Gerakopoulos et al., 2010], is present and can be clearly used as a tool to distinguish a Kerr from a non-Kerr metric.

## References

- Apostolatos, T. A., Lukes-Gerakopoulos, G., & Contopoulos, G. [2009], “How to Observe a Non-Kerr Spacetime Using Gravitational Waves”, *Phys. Rev. Let.* **103**, 111101
- Bender, P., Danzmann P., and the LISA Study Team [1998], “Laser Interferometer Space Antenna for the Detection of Gravitational Waves, Pre-Phase A Report” **MPQ 233** (Garching: Max-Planck-Institut für Quantenoptik)
- Brink, J. [2008], “Spacetime encodings. II. Pictures of integrability”, *Phys. Rev. D.* **78**, 102002
- Contopoulos, G. [1978], “Higher order resonances in dynamical systems”, *Celest. Mech.* **18**, 195
- Contopoulos, G., & Zikides, M. [1980], “Periodic orbits and ergodic components of a resonant dynamical system”, *Astron. and Astrop.*, **90**, 198
- Contopoulos G., Varvoglis H. & Barbanis B. [1987], “Large degree stochasticity in a galactic model”, *Astron. and Astrop.* **172**, 55
- Contopoulos, G. [2002], “Order and chaos in dynamical astronomy” (Springer, Berlin)
- Flanagan, É. É., & Hinderer, T. [2007], “Evolution of the Carter constant for inspirals into a black hole: Effect of the black hole quadrupole”, *Phys. Rev. D.* **75**, 124007
- Gair, J. R., & Glampedakis, K. [2006], “Improved approximate inspirals of test bodies into Kerr black holes” *Phys. Rev. D.*, **73**, 064037
- Gair, J. R., Li, C., & Mandel, I. [2008], “Observable properties of orbits in exact bumpy spacetimes”, *Phys. Rev. D.* **77**, 024035
- Johannsen, T., & Psaltis, D. [2010], “Testing the No-hair Theorem with Observations in the Electromagnetic Spectrum. I. Properties of a Quasi-Kerr Spacetime”, *Astrop. J.* **716**, 187
- Johannsen, T., & Psaltis, D. [2010], “Testing the No-hair Theorem with Observations in the Electromagnetic Spectrum. II. Black Hole Images”, *Astrop. J.* **718**, 446
- Lukes-Gerakopoulos, G., Apostolatos, T. A., & Contopoulos, G. [2010], “Observable signature of a background deviating from the Kerr metric” *Phys. Rev. D* **81**, 124005
- Manko, V. S., & Novikov, I. D. [1992], “Generalizations of the Kerr and Kerr-Newman metrics possessing an arbitrary set of mass-multipole moments”, *Class. Quant. Grav.* **9**, 2477